IEEE Photonics Journal
An IEEE Photonics Society Publication

Open Access

# The Propagation Properties of a Longitudinal Orbital Angular Momentum Multiplexing System in Atmospheric Turbulence

Volume 10, Number 1, February 2018

Qinghua Tian
Lei Zhu
Yongjun Wang
Qi Zhang
Bo Liu
Xiangjun Xin

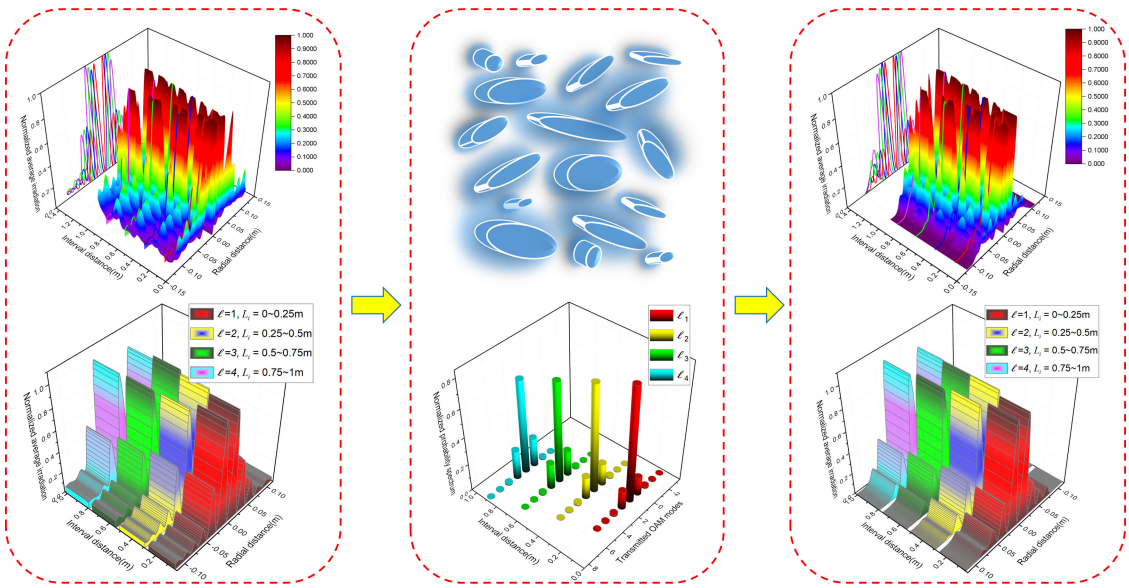


DOI: 10.1109/JPHOT.2017.2778238
1943-0655 

# The Propagation Properties of a Longitudinal Orbital Angular Momentum Multiplexing System in Atmospheric Turbulence

**Qinghua Tian**,[1,2,3] **Lei Zhu**,[1,3] **Yongjun Wang**,[1,2,3] **Qi Zhang**,[1,2,3] **Bo Liu**,[4] **and Xiangjun Xin**[1,2,3]

[1]School of Electronic Engineering, Beijing University of Posts and Telecommunications, Beijing 100876, China
[2]State Key Laboratory of Information Photonics and Optical Communications, Beijing University of Posts and Telecommunications, Beijing 100876, China
[3]Beijing Key Laboratory of Space-Ground Interconnection and Convergence, Beijing University of Posts and Telecommunications, Beijing 100876, China
[4]Academy of Opto-Electronics, Nanjing University of Information Science and Technology, Nanjing 210044, China

*DOI:10.1109/JPHOT.2017.2778238*


Manuscript received October 12, 2017; revised November 21, 2017; accepted November 25, 2017. Date of publication November 29, 2017; date of current version January 5, 2018. This work was supported in part by the National Natural Science Foundation of China under Grant 61575026, in part by the National Science Fund for Distinguished Young Scholars under Grant 61425022, and in part by National High Technology Research and Development Program of China under Grant 2015AA015504. Corresponding author: Qinghua Tian (e-mail: tianqh@bupt.edu.cn).

This paper has supplementary downloadable material available at http://ieeexplore.ieee.org.

**Abstract:** A novel multichannel free-space optical (FSO) communication system based on orbital angular momentum (OAM) carried by frozen waves with different longitudinal patterns is studied in this paper. The longitudinal OAM multiplexing (LOAMM) system is simulated under atmospheric turbulence, which is based on the split-step Fourier transform method and includes multiple random phase screens. The influences of system parameters on the average OAM mode probability densities are analyzed and discussed, such as propagation distance, strength of turbulence, sizes of finite aperture function, OAM mode numbers, and source parameters. It is found that in the limited apertures, the detection probability spectrum of the LOAMM system is inversely proportional to OAM mode numbers, strength of turbulence, and propagation distance. The bit-error rate and aggregate capacities are compared between the traditional OAM-based space-division-multiplexing (OAM-SDM) system with Bessel beams and our proposed LOAMM system. Our work should contribute to proving that the LOAMM system has a number of advantages over the OAM-SDM system in FSO communication.

**Index Terms:** Atmospheric turbulence, free-space optical (FSO) communication, orbital angular momentum (OAM) multiplexing.

## 1. Introduction

Optical communication systems have been developed to satisfy the growing demand for data capacity [1], broadband services [2] and Internet traffic [3]. In recent years, free-space optical (FSO) communication using twisted light for high-data-rate transmission has attracted worldwide

attention. It was shown by G. Gibson *et al.* that vortex beams with OAM have the helical phase front term $\exp(i\ell\varphi)$, where $\ell$ is the topological charge with arbitrary integer, and $\varphi$ is the azimuthal angle [4]. These beams carrying distinct OAM modes exhibit the orthogonality, which can tremendously enhance the channel information capacity of FSO communication systems without increasing the spectral bandwidth [5], [6].

In contrast with fiber-based communication system, FSO communication system relies on the atmosphere or ocean as the transmission medium instead of the physical communication link. Current studies have extensively explored the effects of atmospheric turbulence on vortex beams. The results indicate that the turbulence-induced scintillation significantly limits the development of OAM-based communication system and give rise to channel crosstalk [7]. To mitigate the distortions caused by turbulence, some reasonable methods such as adaptive optics methods [8], [9] and signal processing-based methods [10] have been proposed to improve the performance of OAM-multiplexed systems. Moreover, pure-phase-perturbation approximation and numerical simulations based on split-step Fourier transform method have been widely employed to analyze the turbulence-induced effects on different kinds of vortex beams [11]–[13]. However, there are still a lot of defects in practical FSO communication links with proposed OAM-based multiplexing system. Due to the noise and intermodal crosstalk, the theoretically infinite number of modes is impossible and the OAM-based-multiplexed systems are generally designed with larger mode spacing [14]. Furthermore, as the topological charges increase, the beam divergence begins to intensify and the receiver aperture should be designed to maintain the sizes of beams [15].

Recently, some attentions have been paid to a class of non-diffracting beams known as Frozen waves (FWs), which were first put forward by Zamboni-Rached [16], [17]. These waveforms are composed of co-propagating Bessel beams, which have equal-frequency but different longitudinal wave numbers. In contrast with other non-diffracting beams, FWs have an ability to control the transverse intensity patterns as well as longitudinal intensity pattern. This focusing property of FWs have been employed in many fields, such as optical trapping and micromanipulation [18], [19]. In 2016, Dorrah *et al.* first proposed a novel model of FWs, where the sign and value of topological charges are controllable along the propagation axis in a short distance [20]. Inspired by this characteristics of FWs mentioned above, we establish a longitudinal OAM-multiplexing (LOAMM) system by application of FWs to overcome the shortcomings aforementioned. In this model, the OAM modes are divided into independent intervals along beam axis as carriers.

In this paper, the effects of atmospheric turbulence on the LOAMM system are investigated in detail. Our main goal is to explore the factors which shall be considered in the design of the LOAMM system and analyze the properties and aggregate capacity of the system. Firstly, we formulate the transmission model and derive the average mode probability densities of the LOAMM system in turbulence. Numerical simulations based on split-step Fourier transform with random multiple phase screens are applied to produce graphical results. The normalized density probability spectrum (DPS) and crosstalk probability spectrum (CPS) with closed-form expressions are derived. Then, we verify the accuracy of transmission model in turbulence and analyze the influences of source parameters on the DPS of the LOAMM system in different turbulence strength. The results from the numerical simulations are verified by comparison with analytical solutions derived by Rytov approximation. Furthermore, we model each OAM mode as a binary symmetric channel and derive BER and aggregate capacity according to the value of signal-to-noise ratio (SNR) per channel. Finally, we compare the aggregate capacity of the traditional OAM-SDM system based on Bessel beams, with the proposed LOAMM system in the same conditions. The results reveal that the LOAMM system outperforms the OAM-SDM system only in the condition that the channel capacity is saturated. It provides a new guideline for designing practical multiplexing systems in FSO communication links.

## 2. Transmission Model of LOAMM System

In previous works, the FWs have been experimentally demonstrated over meter or micrometer space regions [16]–[19]. However, in this paper, the LOAMM system is not limited in a short-range research. The theoretical model is proved to yield periodic waveforms in principle. In FSO

communication links without atmospheric turbulence, the LOAMM system based on FWs can be expressed as [20]

$$\Psi_{\ell m}^{(0)}(r, \varphi, z, t) = \exp(-i\omega t) \sum_{\ell=-\infty}^{\infty} \sum_{m=-N}^{N} A_{\ell m} \exp(ik_{z\ell m} z) J_{\ell}(k_{r\ell m} r) \exp(i\ell\varphi) \tag{1}$$

where $m$ is the sum of a superposition of Bessel beams. The Bessel beams are composed of equal-frequency $\omega$ and different longitudinal wave numbers $k_{z\ell m}$. The complex coefficient $A_{\ell m}$ represents weighting factor, which can be regarded as a series of Fourier-like coefficients of the desired longitudinal pattern $|F_{\ell}(z)|^2$ over a finite distance $L$ and written as

$$A_{\ell m} = \frac{1}{L} \int_0^L F_{\ell}(z) \exp\left( -i \frac{2\pi m}{L} z \right) dz \tag{2}$$

Here the $F_{\ell}(z)$ can be expanded into an Fourier-like series (FS) with selected $k_{z\ell m}$ [16]

$$F_{\ell}(z) \cong \sum_{m=-N}^{N} A_{\ell m} \exp(ik_{z\ell m} z) \tag{3}$$

where the $k_{z\ell m} = Q + 2\pi \mathrm{m}/L$ indicates longitudinal wave numbers and $Q$ is a constant value that determines the degree of transverse field of localization.

However, the desired longitudinal pattern $|F_{\ell}(z)|^2$ is not limited to finite distance $L$, because the coefficients $A_{\ell m}$ are discrete aperiodic sequences with the form of sinc-like function and totally contain $2N + 1$ sampling values. For this reason, the FWs can transmit along the axis as periodic waveforms with the period of $L$. Due to the unique properties, the OAM modes carried by FWs can be divided into separated finite space intervals. By adjusting $F_{\ell}(z)$ and $L$, we denote the field distributions of a LOAMM system with desired topological charges. The simple model of the LOAMM system is presented in Fig. 1, accompanied with a superposition of M-multiplexed FWs.

Similar to the method described in [21], the system is split into four channels as an example. Each channel carrying modulated signals is characterized by a specific FW state with desired topological charge as depicted in Fig. 1(a). By a superposition of each FW state, all the modulated signals are transmitted coaxially and simultaneously through free space. The selected FWs with desired topological charges have effective contributions to the beam center over a finite space interval and then switch off when propagating out of the region. It should be noted that the OAM of the entire waveform is conserved, while all the OAM states are not present at the same time. When the state of FW is switched off, its energy (momentum) is dispersed over a larger space in the outer rings and can be restored back after a period of $L$ as shown in Fig. 1(b). We first choose a short interval (15 cm) between each FWs states [showed as the left graph in Fig. 1(c)] and they are not connected serially. However, the longitudinal intensity profiles of the FWs fluctuate violently, which will have a terrible influence on the detection accuracy. Due to the stability and reliability of the LOAMM, the beams are generated by superposition of each FW using the longitudinal structural function $F_{\ell}(z)$ over length $L = 100$ cm [showed as the right graph in Fig. 1(c)] with 25 cm as the interval,

$$F_{\ell}(z) = \begin{cases} F_{\ell_1} = 1, & 0 \text{ cm} \le z \le 25 \text{ cm} \\ F_{\ell_2} = 1, & 25 \text{ cm} \le z \le 50 \text{ cm} \\ F_{\ell_3} = 1, & 50 \text{ cm} \le z \le 75 \text{ cm} \\ F_{\ell_4} = 1, & 75 \text{ cm} \le z \le 100 \text{ cm} \end{cases} \tag{4}$$

The transverse intensity profiles of waveforms located at $z = 15, 40, 65, 90$ cm are illustrated in Fig. 1(d). The results from probing nodes represent the physical characteristics of each channel. In practical FSO communication system, the combination of polarization beam splitter (PBS) and CCD camera are effective method to receive the FWs.

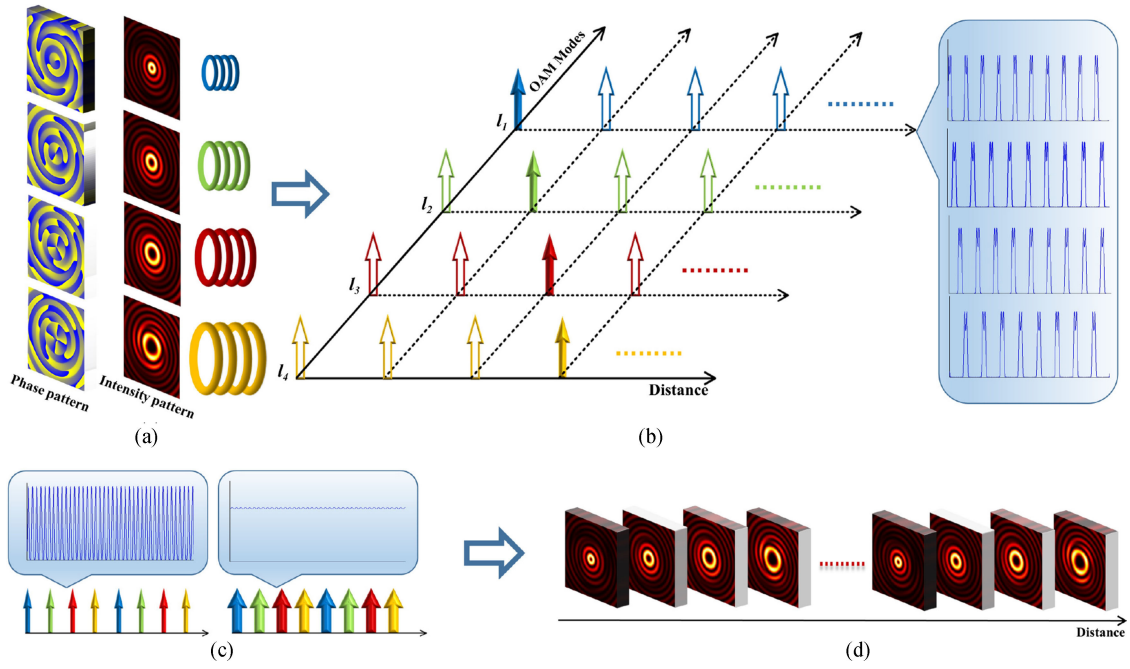


Fig. 1. The model of LOAMM system. The topological charges of the system range from $\ell_1$ to $\ell_4$. (a) Phase and intensity distribution of the system obtained from four nodes in each interval. (b) The longitudinal structure of each channel over a distance of $L = 100$ cm. (c) The longitudinal intensity of FWs with different intervals. (d) The superposition of each FW propagation with a periodic pattern through free space (see the simulated FWs dynamics in Visualization 1).

## 3. Theoretical Expression of Turbulence-Induced Effects on LOAMM System

Extended Huygens-Fresnel (EHF) principle is employed to simulate the turbulence-induced effect on single channel of the LOAMM system with FWs in FSO links. We consider that the FWs propagate along the axis perpendicular to the transverse field from the source plane of $z = 0$ cm to $z = 100$ cm to the observation plane at $z' = L_d$ cm to $z' = L_d + 100$ cm. The transmitted beams are aligned with the received beams, which means there is no angular deflection and location offset during transmission. The waveform field distribution at the observation plane can be expressed by [22]

$$\Psi_{\ell m}(\boldsymbol{r}, z') = \frac{k}{2\pi i L_d} \exp(ikL_d) \iint d^2\boldsymbol{\zeta} \Psi^{(0)}_{\ell m}(\boldsymbol{\zeta}, z) \left[ \exp \frac{ik|\boldsymbol{r} - \boldsymbol{\zeta}|^2}{2z} + \psi(\boldsymbol{r}, \boldsymbol{\zeta}, z) \right] \tag{5}$$

where $\boldsymbol{\zeta} = (\zeta, \varphi) = (x, y)$ is the two-dimensional point in the source plane, $\boldsymbol{r}$ is the point at the observation plane; $L_d$ denotes the propagation distance; $\psi(\boldsymbol{r}, \boldsymbol{\zeta}, z)$ represents the complex phase of waves impaired by turbulence when propagating from the source point $(\boldsymbol{\zeta}, z)$ to the observation point $(\boldsymbol{r}, z')$. $\Psi^{(0)}_{\ell m}(\boldsymbol{\zeta}, z)$ stands for the normalized complex amplitude of the FWs given by Eq. (1). The field derived from Eq. (5) can be expanded into the form [23]

$$\Psi_{\ell m}(\boldsymbol{r}, z') = \sum_{\ell'=-\infty}^{\infty} c_\ell(\ell') \Psi^{(0)}_{\ell' m'}(\boldsymbol{r}, z') \tag{6}$$

where

$$c_\ell(\ell') = \int_0^{2\pi} \int_0^{\infty} \Psi_{\ell m}(\boldsymbol{r}, z') \Psi^{(0)*}_{\ell' m'}(\boldsymbol{r}, z') r dr d\varphi \tag{7}$$

It should be noted that $\Psi^{(0)*}_{\ell' m'}(\boldsymbol{r}, z')$ is the field of normalized FWs states at the observation plane without atmospheric turbulence. The average mode probability density of the FWs can be expressed as

$$q_\ell(\ell') = \left\langle \left| c_\ell(\ell') \right|^2 \right\rangle \tag{8}$$

By substituting Eq. (7) into Eq. (8), we can obtain $q_\ell(\ell')$ as

$$q_\ell(\ell') = \iint d^2\tilde{\boldsymbol{r}} \iint d^2\tilde{\boldsymbol{r}}' \tilde{\Gamma}_\ell(\tilde{\boldsymbol{r}}, \tilde{\boldsymbol{r}}', z') \tilde{\Gamma}^{(0)}_\ell(\tilde{\boldsymbol{r}}, \tilde{\boldsymbol{r}}', z') \tag{9}$$

where $\tilde{\Gamma}_\ell(\tilde{\boldsymbol{r}}, \tilde{\boldsymbol{r}}', z')$ represents mutual coherence function for the wave field and can be described by Eq. (10) as

$$\tilde{\Gamma}_\ell(\tilde{\boldsymbol{r}}, \tilde{\boldsymbol{r}}', z') = \left(\frac{k}{2\pi L_d}\right)^2 \iint d^2\boldsymbol{\zeta} \iint d^2\boldsymbol{\zeta}' \Gamma^{(0)}_\ell(\boldsymbol{\zeta}, \boldsymbol{\zeta}') \left[ \exp\left( \frac{ik\left|\boldsymbol{\zeta} - \tilde{\boldsymbol{r}}\right|^2}{2L} \right) - \exp\left( \frac{ik\left|\boldsymbol{\zeta}' - \tilde{\boldsymbol{r}}'\right|^2}{2L} \right) \right]$$
$$\times \exp\left[ -\frac{\hat{r}^2 + \hat{\boldsymbol{r}} \times \hat{\boldsymbol{\xi}} + \hat{\xi}^2}{\rho_0^2} \right] \tag{10}$$

where $\hat{\boldsymbol{r}} = \tilde{\boldsymbol{r}} - \tilde{\boldsymbol{r}}'$ and $\hat{\boldsymbol{\xi}} = \boldsymbol{\zeta} - \boldsymbol{\zeta}'$, $\hat{r} = |\hat{\boldsymbol{r}}|$ and $\hat{\xi} = |\hat{\boldsymbol{\xi}}|$. The spatial coherence radius of spherical waves $\rho_0 = (0.55 C_n^2 k^2 L_d)^{-3/5}$, where $C_n^2$ denotes the structure constant. $\Gamma^{(0)}_\ell(\boldsymbol{\zeta}, \boldsymbol{\zeta}') = \Psi^{(0)}_{\ell m}(\boldsymbol{\zeta}, z) \Psi^{(0)*}_{\ell m'}(\boldsymbol{\zeta}', z)$ indicates the mutual coherence function of normalized wave field at the source plane and the asterisk* implies the complex conjugate.

The theoretical results obtained from Eq. (9) are difficult to simulate analytically because it contains high-dimensional integrals. For this reason, numerical simulations based on split-step Fourier transform method inserting into multiple random phase screens are used to generate propagated wave fields. The turbulence model employed in this paper is based on modified Von Kármán spectrum. We set the number of random phase screens within the range from 11 to 21 according to the turbulence strength [24]. The transverse intensity profiles of FWs with $\ell' = +1$ are depicted at the bottom of Fig. 2. It can be noticed from the picture that the intensity profile deteriorates as the strength of turbulence increases. However, the theoretical model cannot be physically realizable since the Bessel beam has infinite power extent [25], [26]. Due to this reason, a finite aperture function known as super-Gauss function is decided to be added to beams as follows [27]

$$G_{sg}(x, y) = \exp\left[ -\left( \frac{r}{\alpha \delta N} \right)^n \right] \tag{11}$$

where, $n = 16$ means the order of function and $\alpha$ is a parameter that specifies the width of the tapered region. In addition, the sizes of the aperture function have a tremendous effect on the average mode probability density of the system, which has been discussed in the next section. The schematic diagram of the propagation characteristics of the LOAMM system is indicated in Fig. 3. As shown in Fig. 1(b) and the supplemental material visualization 1, the intensity of waveform in transition from one state to another state is not stable. The detection efficiency will not be affected obviously unless the planes are located in the transition interval. As a result, the topological charges of the exampled system are chosen from $+1$ to $+4$ with the longitudinal interval of 25 cm and the refractive-index structure constant $C_n^2 = 1 \times 10^{-16}\,\mathrm{m}^{-2/3}$.

The normalized probability spectrum of the numerical simulation can be calculated with azimuthal number $\ell$ as follows

$$C_\ell(\ell') = \frac{\int_{-\infty}^{\infty} q_\ell(\boldsymbol{r}, \ell') r dr}{\sum_{p=-\infty}^{\infty} \int_{-\infty}^{\infty} q_p(\boldsymbol{r}, \ell') r dr} = \frac{\int_{-\infty}^{\infty} q_\ell(\boldsymbol{r}, \ell') dx dy}{\sum_{p=-\infty}^{\infty} \int_{-\infty}^{\infty} q_p(\boldsymbol{r}, \ell') dx dy} = \frac{\sum_{m=-N}^{N} \sum_{n=-N}^{N} q_\ell(m, n, \ell')}{\sum_{p=-\infty}^{\infty} \sum_{m=-N}^{N} \sum_{n=-N}^{N} q_p(m, n, \ell')} \tag{12}$$

where $m, n$ indicate the grid number of $x, y$ axis, respectively at the observation plane, which is composed of $N \times N$ grids. In the case of $\ell = \ell'$, $C_\ell(\ell')$ denotes the normalized DPS, which means

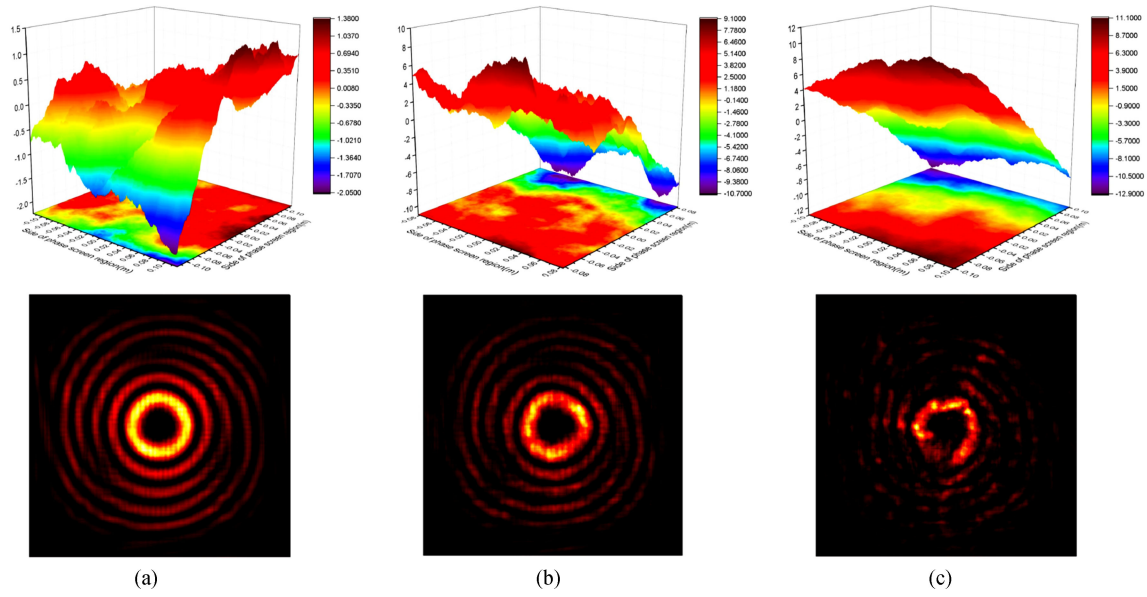

(a) (b) (c)

Fig. 2. Phase screens realizations with different refractive-index structure constant parameters and transverse intensity profiles with $\ell' = +1$. (a) $C_n^2 = 1 \times 10^{-16}\,\mathrm{m}^{-2/3}$. (b) $C_n^2 = 1 \times 10^{-15}\,\mathrm{m}^{-2/3}$. (c) $C_n^2 = 1 \times 10^{-14}\,\mathrm{m}^{-2/3}$. Only one simulated field realization is used to obtain a graphical result.

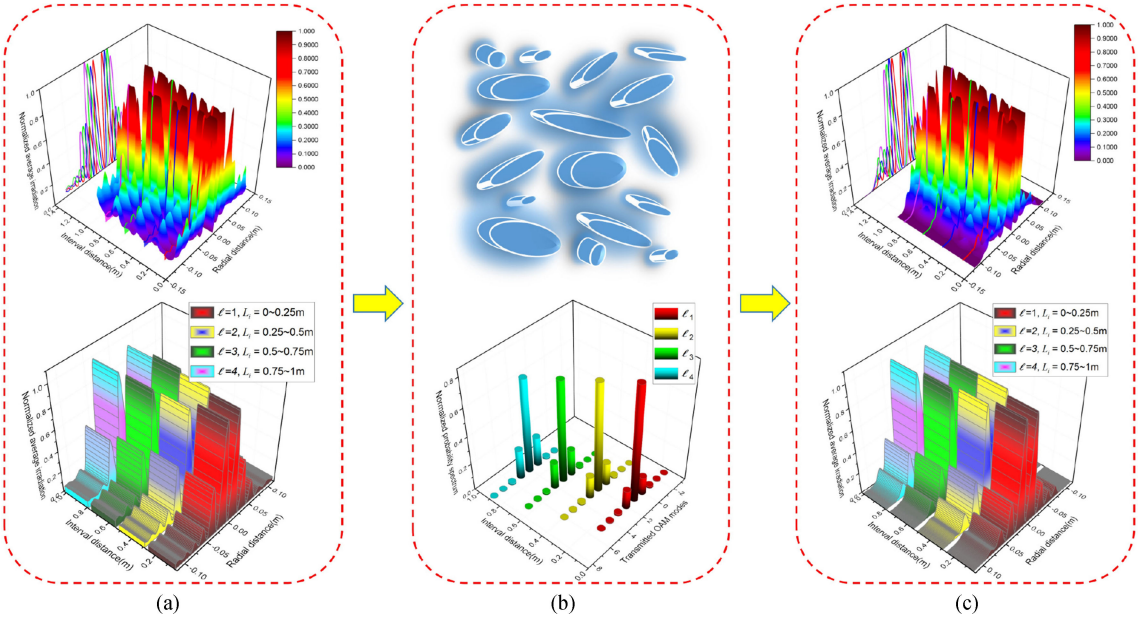


(a) (b) (c)

Fig. 3. The concept of FSO communication link in turbulence using LOAMM system carrying FWs. The topological charges range from $+1$ to $+4$ with the longitudinal interval of 25 cm. To obtain average graphical results, 1000 simulated field realizations are used to obtain 3D profiles. (a) The 3D normalized average irradiance of LOAMM system in the absence of atmospheric turbulence. We select $z = 15, 40, 65, 90$ cm respectively as source plane. Each intensity profile chosen as a sample value for this interval is expanded into the whole interval as depicted in the lower part of (a). (b) The effects of atmospheric turbulence with refractive-index structure constant $C_n^2 = 1 \times 10^{-16}\,\mathrm{m}^{-2/3}$ and aperture function on LOAMM system. The ideal four OAM modes are break down into adjacent modes (c). The 3D normalized average irradiance of LOAMM system in the presence of atmospheric turbulence. Other values adopted in this figure are the same with (a).

the signal power reserved in transmitted OAM mode. In the case of $\ell \neq \ell'$, $C_\ell(\ell')$ means the normalized CPS induced by turbulence, which represents the probability of transmitted energy from signal channel spreading into other channels.

The transmission model of FWs in atmospheric turbulence makes it capable of evaluating the channel capacity of the LOAMM system by a simple approach based on detection model and crosstalk model described above. Here, we establish a LOAMM system composed of *M*-OAM channels. Each constituent channel $\eta \in \boldsymbol{O}$ is modeled as binary-symmetric and independently addressable. Therefore, the statistic characteristics between channels are independent of each other. The noise added to the receiver noise can be regarded as an independent Gauss noise introduced by crosstalk. As a result, the receiver noise can be modeled as additive white Gauss. Thus, the signal-to-noise ratio (SNR) can be expressed as [13]

$$\gamma = \frac{C^2_{\ell=\ell'}(\ell')}{\sum_{\eta\in\boldsymbol{O}}^{\eta\neq\ell'} C^2_\eta(\ell') + \frac{N_0}{P_{Tx}}} \tag{13}$$

where $C^2_{\ell=\ell'}(\ell')$ is the DPS and $C^2_\eta(\ell')$ is normalized CPS as described above. $N_0$ denotes the receiver noise, $P_{Tx}$ represents transmitted power. For orthogonal modulation formats, such as on/off key (OOK) and binary pulse position modulation (PPM), the aggregate capacity of LOAMM system in FSO communication link with turbulence can be calculated by

$$C = \sum_{\ell'\in\boldsymbol{O}} C\left(\sigma_{\ell'}\right) \tag{14}$$

with

$$C\left(\sigma_{\ell'}\right) = 1 + \sigma_{\ell'}\log_2\sigma_{\ell'} + \left(1-\sigma_{\ell'}\right)\log_2\left(1-\sigma_{\ell'}\right) \tag{15}$$

$$\sigma_{\ell'} = \frac{1}{2}\,\mathrm{erfc}\left(\sqrt{\frac{\gamma}{2}}\right) \tag{16}$$

where $C(\sigma_{\ell'})$ represents the capacity of binary-symmetric channel (BSC), $\sigma_{\ell'}$ denotes the BER for desired channel $\ell'$ and erfc(.) represents the complementary function.

## 4. Simulation and Discussion

In this section, we discuss the design considerations and analyze the propagation properties as well as the channel aggregate capacity of the LOAMM system in atmospheric turbulence. The focus of this paper is mainly on investigating the normalized DPS and CPS under the following variations: the propagation distance, the topological charges, the finite aperture function's sizes, the structure constant of refractive-index and the number of a superposition of Bessel beams. The parameters of numerical calculations are assumed unless otherwise specified: the wavelength $\lambda = 532$ nm, the topological charges are chosen from $\ell' = +1$ to $\ell' = +4$, the length of periodic waves $L = 100$ cm, the longitudinal interval of each OAM mode is 25 cm, the transverse function constant $Q = 0.9999958k$, the morphological function $F_\ell(z) = 1$ in any interval region, the turbulence outer scale $L_0 = 100$ m and the inner scale $\ell_0 = 0.0001$ m. The total array size is $1024 \times 1024$ pixel$^2$ at the source plane, the observation plane and the partial propagation plane, respectively. The results obtained from simulations repeat 1000 times totally to get a mean measurement.

Due to the properties of the beam itself, the sizes of FWs is too small to maintain the mode spacing of Fourier transform [24]. Therefore, a beam expander should be placed behind the laser beam emitter. However, the DPS of transmitted OAM modes will be more dispersive as the beam waist expands. In order to satisfy the constraints simultaneously, the initial grid spacing is set to $\delta_0 = 1.12 \times 10^{-6}$ m and the parameter of magnification are 204, 177, 144 for the corresponding refractive-index structure constant $C_n^2 = 1 \times 10^{-16}, 1 \times 10^{-15}, 1 \times 10^{-14}\,\mathrm{m}^{-2/3}$, respectively.

### 4.1 Verification of Accuracy for Numerical Simulation Process in Atmospheric Turbulence

In our numerical simulation model, the simulation process has been repeated 1000 times to obtain the average irradiance distribution. To confirm that the numerical simulation process matches the analytical formulae, we first compare the normalized average irradiance distribution of FWs with $\ell' = +1$ at the observation plane derived by numerical simulation and that computed by analytical solutions. In this sub-section, $\alpha$ is set to 0.47 to remain the main lobe and first side lobe to get explicit and clear graphical results. The normalized average irradiance of FWs can be represented by [28]

$$\begin{aligned} \langle I_{\ell m}(\boldsymbol{r}, z')\rangle &= F^{-1}\left\{F\left[I_{\ell m}^{(0)}(\boldsymbol{r}, z')\right] F\left[\xi(\boldsymbol{r}, z')\right]\right\} \\ \langle \tilde{I}_{\ell m}(\boldsymbol{r}, z')\rangle &= \frac{\langle I_{\ell m}(\boldsymbol{r}, z')\rangle}{\max\left\{\langle I_{\ell m}(\boldsymbol{r}, z')\rangle\right\}} \end{aligned} \tag{17}$$

where $I_{\ell m}^{(0)}(\boldsymbol{r}, z') = \Psi_{\ell m}^{(0)}(\boldsymbol{r}, z')\Psi_{\ell m}^{(0)*}(\boldsymbol{r}, z')$ is the intensity distribution of the field at the observation plane in the absence of turbulence, $F^{-1}$ is the inverse Fourier transform and $F[\xi(\boldsymbol{r}, z')]$ is the Fourier transform of a point spread function that can be expressed as [28]

$$F\left[\xi(\boldsymbol{r}, z')\right] = \exp\left[-\frac{1}{2} D_{sp}\left(\kappa \frac{L_d}{k}\right)\right] \tag{18}$$

with [29]

$$D_{sp}(r) \cong 1.093 C_n^2 k^2 L_d \ell_0^{-1/3} r^2 \left\{\left[1 + (r/\ell_0)^2\right]^{-1/6} - 1.319(\ell_0/L_0)^{1/3}\right\} \tag{19}$$

where $D_{sp}(.)$ represents the spherical wave structure function and $\kappa$ denotes the spatial frequency vector. The irradiance patterns and the comparison of normalized average irradiance curves between numerical simulation and that computed by analytical solutions are depicted in Fig. 4. It can be found that the results of the two approaches are in a good agreement when $C_n^2 = 1 \times 10^{-16}\,\mathrm{m}^{-2/3}$ and $1 \times 10^{-15}\,\mathrm{m}^{-2/3}$ except for a little deviation at the peaks of the side lobes. The difference is caused by the fact that the selected node is in an interval, in which the sampling results cannot significantly match the average results. The deviation will diminish or even vanish if more transverse profiles from different nodes are averaged. In the condition of $C_n^2 = 1 \times 10^{-14}\,\mathrm{m}^{-2/3}$, the error between two curves increases. Due to the distribution calculated by a finite number of simulated realizations, the difference is obvious. The curves of the two approaches will match more closely if more calculated results are averaged. Therefore, the transmission model through turbulence established by numerical simulations is credible.

### 4.2 Design Considerations and Properties Analysis Based on DPS and CPS

In order to verify the accuracy of results obtained from numerical simulations, an analytical example derived from Refs. [11], [31], and [32] is used as comparison. Firstly, the effects of propagation distance on the normalized probability spectrum are analyzed. The accuracy of DPS and CPS are verified by comparison between detailed data obtained from numerical simulation and that computed by analytical solutions based on Rytov approximation, separately. The Rytov approximation is only valid under weak fluctuations associated with the Rytov variance $\sigma_\ell^2 < 1$ [30]. The atmospheric turbulence reaches its maximum value in the case of $C_n^2 = 1 \times 10^{-14}\,\mathrm{m}^{-2/3}$ and $L_d = 1000$ m. Obviously, the Rytov variance $\sigma_\ell^2 = 1.23 C_n^2 k^{7/6} L_d^{11/6} \approx 0.69$ meets the constraints well. Fig. 5 shows the DPS and CPS of the LOAMM system as a function of distance $L_d$. The crosstalk changes from OAM state $\ell'$ to $\ell'+1$. The propagation distance ranges from 0 m to 1000 m, and the parameter of aperture function $\alpha = 0.47$. The solid curves represent the analytical solutions (AS), whereas the dotted curves denote numerical simulation results (NS). It can be seen from the picture that the curves of the two approaches are in a good consistency, but not complete coincidence. It is obvious that as the distance increases, the DPS decreases and the CPS increases. The curves of DPS

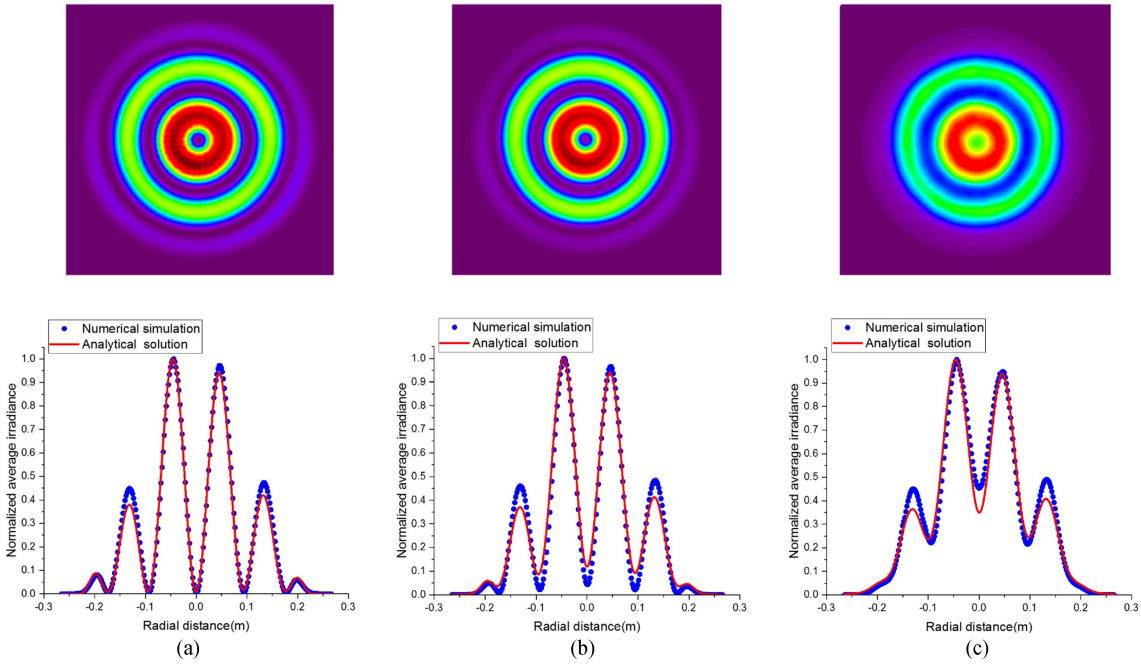


Fig. 4. The normalized average irradiance distribution of FWs with $\ell' = +1$ propagating through turbulence in the condition of different $C_n^2$, (a) $C_n^2 = 1 \times 10^{-16}\,\mathrm{m}^{-2/3}$, (b) $C_n^2 = 1 \times 10^{-15}\,\mathrm{m}^{-2/3}$, (c) $C_n^2 = 1 \times 10^{-14}\,\mathrm{m}^{-2/3}$. The irradiance curves and the transverse profiles of normalized average irradiance patterns are depicted in the picture, respectively. The dotted curves represent analytical solution shown in Eq. (17), whereas the solid curves represent numerical simulation results obtained from the upper patterns. The averaged value is calculated from 1000 samples.

and CPS tend to merge together when the $C_n^2 = 1 \times 10^{-14}\,\mathrm{m}^{-2/3}$. The results are consistent with the [31] and [32] that the performance of the LOAMM system becomes worse as the propagation distance become larger.

In the published papers, the sizes of aperture function added on the Laguerre-Gauss (LG) beam have been discussed in detail [33]–[36]. According to [37], the aperture function's radius of Bessel beams are investigated. The power from the central peak up to the first zero is contained, in which the Bessel beams are considered to be generated with 100% of the laser power. In this subsection, we analyze the effects of aperture function's sizes of source plane (SP) and observation plane (OP) on the DPS and choose the suitable parameter of $\alpha$ for the design of the LOAMM system. In the condition of $L_d = 1000$ m and refractive-index $C_n^2 = 1 \times 10^{-14}\,\mathrm{m}^{-2/3}$, the normalized DPS of transmitted OAM modes, as a function of the parameter of $\alpha$, is shown in Fig. 6. The energy in transmitted OAM mode is dispersive significantly as the topological charge increases. The peak height of the 3D histogram denotes that the transmitted FWs have an optimal DPS when the aperture function contains the main lobe of FWs exclusively. According to the results obtained from simulation model and existing literatures mentioned above, the sizes of the aperture function in our simulations can be considered to include both power efficiency and detection efficiency. In the source plane, if the size of aperture is not large enough to contain the waveforms with the largest number of OAM states, the FWs will not transmit along the propagation direction as periodic waveforms. Moreover, if the aperture function is added on the source plane, all the waveforms will not be received through the suitable aperture function except the beam carrying the largest OAM state. Then the detection efficiency will not be the best. At the observation plane, the FWs can be received and detected separately, which denotes that the waveforms carrying different OAM states can be detected in a suitable aperture sizes. In Fig. 6, the condition of SP and OP are considered, respectively. In the next subsection, the DPS and CPS will be discussed only in the condition of

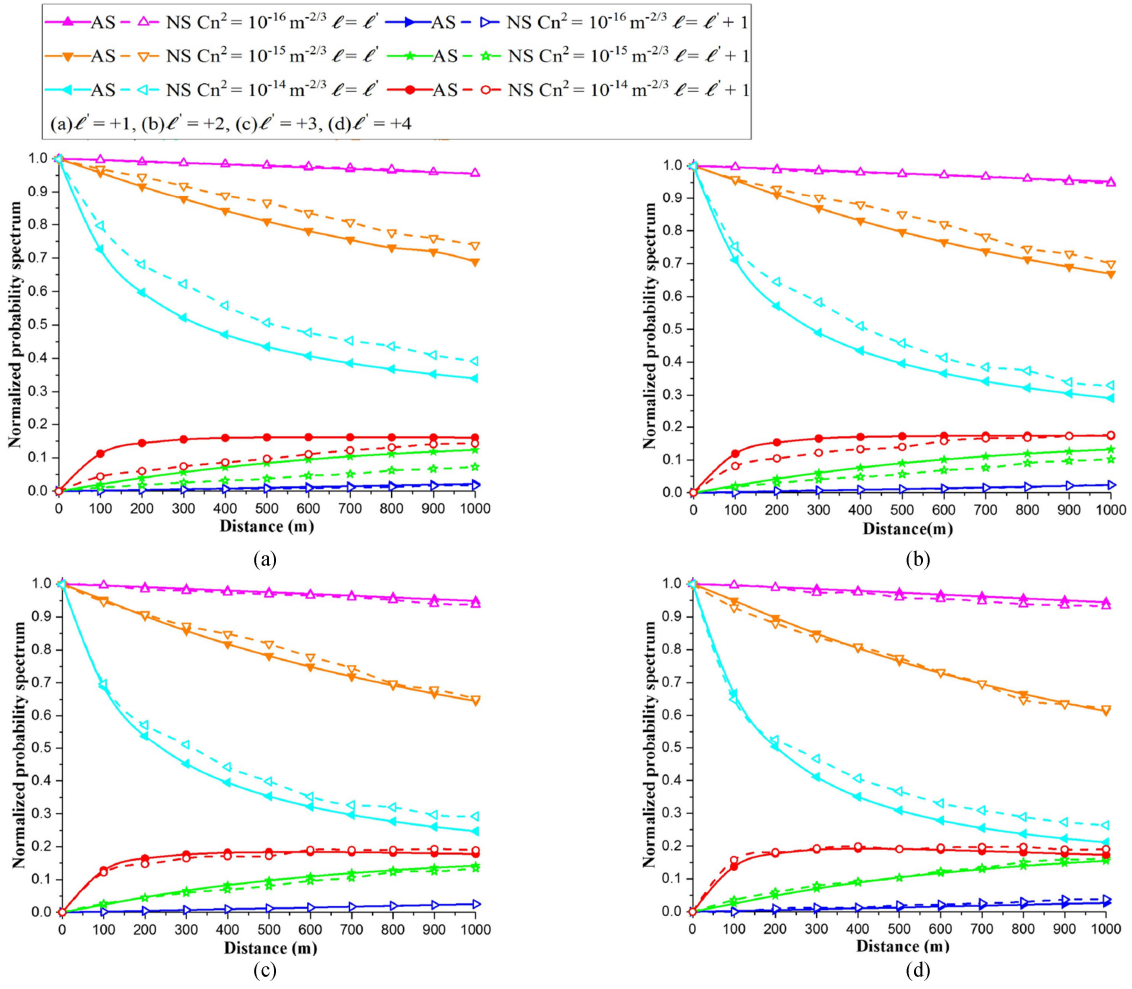


Fig. 5. The normalized DPS and CPS of the LOAMM system in turbulence with the refractive-index structure constant $C_n^2 = 1 \times 10^{-16}, 1 \times 10^{-15}, 1 \times 10^{-14}\,\mathrm{m}^{-2/3}$, separately and the parameter of aperture function $\alpha = 0.47$, as a function of the propagation distance $L_d$.

OP. We will consider the aperture of SP and OP on analyzing the channel capacity in the next section.

Furthermore, the changes in the DPS against the parameter $N$ of Bessel beams' number $m = 2N + 1$, which are superimposed to form the FWs, are investigated in Fig. 7. In this context, the $\alpha = 0.17, 0.22, 0.27, 0.32$ stand for the $\ell' = +1, +2, +3, +4$, respectively, the $C_n^2 = 1 \times 10^{-14}\,\mathrm{m}^{-2/3}$ and the $L_d = 1000$ m. Similar to Fourier series expansion, the states of FWs at a sampling point can be restored better with more equal-frequency Bessel beams. However, the upper limit of parameter $N$ is 8 in this paper because the condition $0 \leq Q + 2\pi m/L \leq \omega/c$ should be satisfied to ensure only forward propagation is included [16]. It is evident that the morphological function $F_\ell(z)$ consists of $2N + 1$ coefficients $A_{\ell m}$ and the upper limit of Bessel beams is 17. It is clear that the DPS increases as the beam number increases and tends to be stable when the beam number closes to the upper bound.

At last, the influences of OAM mode numbers on normalized probability spectrum are examined. As shown in Fig. 8, for the fixed beam number $m = 7$, parameter of aperture function $\alpha = 0.17, 0.22, 0.27, 0.32, 0.37, 0.42, 0.47, 0.52, 0.57, 0.62, 0.67, 0.72, 0.77$ for topological charges $\ell'$ range from 0 to +13 and other parameters with the same values used in Fig. 7. It is obvious that the DPS decreases with increasing OAM mode numbers, but meanwhile the CPS increases. The

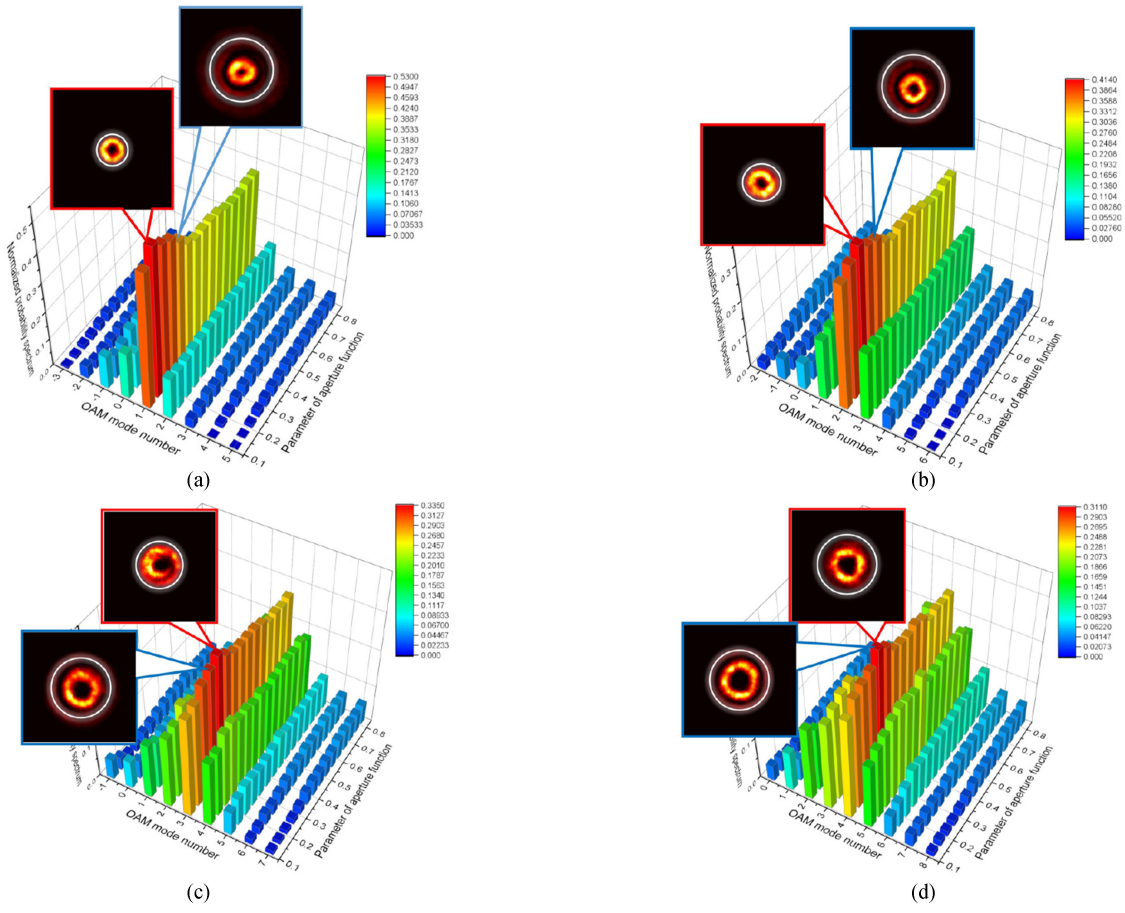


Fig. 6. The effects of the parameter of the aperture function $\alpha$ on the DPS. The red frame denotes the condition of OP and the blue frame denotes the condition of SP. The distance $L_d = 1000$ m and the refractive-index structure constant $C_n^2 = 1 \times 10^{-14}$ m$^{-2/3}$. The transmission system with topological charges are (a) $\ell' = +1$, (b) $\ell' = +2$, (c) $\ell' = +3$, (d) $\ell' = +4$.

results are consistent with the [12], [13], [21], and [31] that the transmitted OAM modes spread into adjacent modes more dramatically as the topological charges increase. Similar to Fig. 5, the normalized probability spectrum curves derived by numerical simulations and analytical solutions respectively are in a good agreement. The curves between the two approaches have a higher degree of coincidence after the suitable aperture sizes and numbers of Bessel beams are chosen. The errors of the CPS between the two approaches appear greater as the topological charge increases. One of the reasons for this phenomenon is that when the radius containing the main lobe of FWs increase faster, some energy from the detecting OAM modes will be excluded by the aperture function. Another reason is that the field distribution is simulated by averaging only a finite number of realizations.

### *4.3 Analysis of BER and Aggregate Capacity*

Based on the analysis of design considerations and properties of the LOAMM system in Section 4.2, we take a simpler method to calculate the BER and the aggregate capacity, in which the information rate is maximized and only the capacity bound is considered. We first analyze the BER and channel capacity of single independent channel. The topological charges are from $\ell' = 0$ to $\ell' = 10$ and the BER and channel capacity are calculated based on Eqs. (13)–(16) by introducing the DPS and

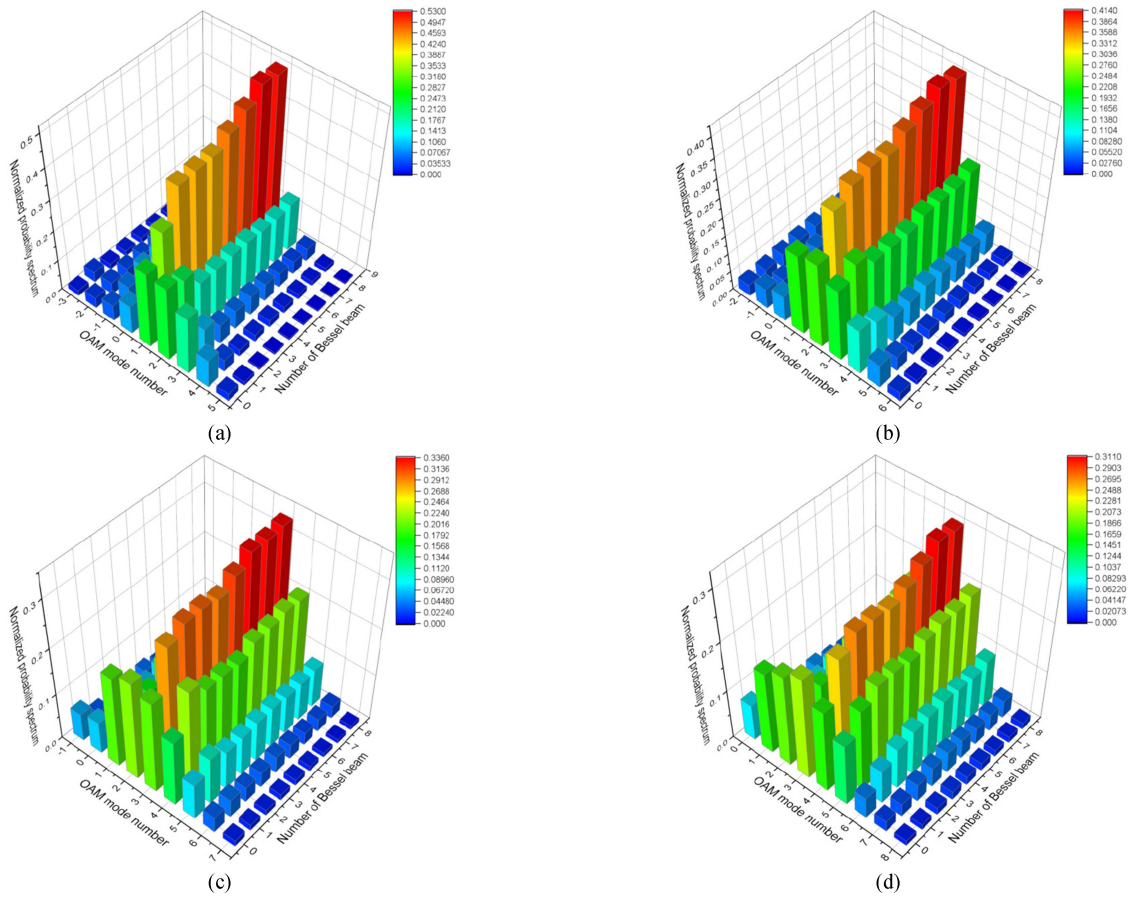


Fig. 7. The effects of the Bessel beam's number $m$ in Eq. (1) on the normalized DPS. The distance $L_d = 1000$m and the refractive-index structure constant $C_n^2 = 1 \times 10^{-14}\,\mathrm{m}^{-2/3}$. The transmission system with topological charges and the parameter of aperture function are (a) $\ell' = +1, \alpha = 0.17$, (b) $\ell' = +2, \alpha = 0.22$, (c) $\ell' = +3, \alpha = 0.27$, (d) $\ell' = +4, \alpha = 0.32$.

CPS discussed in Fig. 8. Then, the comparison of the aggregate capacity between the OAM-SDM system and the LOAMM system is made to verify the advantages of the LOAMM system. There are three sets of OAM-SDM examples, $O_1 = \{+1, +2, +3, +4\}$, $O_2 = \{+1, +3, +5, +7\}$ and $O_3 = \{+1, +4, +7, +10\}$. Two sets of LOAMM systems are selected as examples, $U_1 = \{+1, +2, +3, +4\}$ and $U_2 = \{+1, +1, +1, +1\}$. The BER and aggregate capacity are calculated as a function of $P_{Tx}/N_0$.

Fig. 9 depicts the BER and channel capacity under different aperture conditions, as a function of $P_{Tx}/N_0$ in single channel. It is evident that the system has a good performance with low $P_{Tx}$ requirements when $C_n^2 = 1 \times 10^{-16}\,\mathrm{m}^{-2/3}$ and the BER and channel capacity between different OAM modes differ not greatly as depicted in (a) and (d). As the $P_{Tx}/N_0$ increases, the channel capacity increases until the saturation 1 (bit/channel) is reached. Deteriorations in the condition of $C_n^2 > 1 \times 10^{-16}\,\mathrm{m}^{-2/3}$ are apparent, especially if $\ell' \geq +4$. It is obvious for this phenomenon because the DPS decreases as the topological charges increase. For the case of $\ell' \geq +7$ with $C_n^2 = 1 \times 10^{-14}\,\mathrm{m}^{-2/3}$, the differences of BER and channel capacity among the constituent channels with different OAM modes are not significant. This phenomenon is reasonable because in the condition of $\ell' \geq +7$ with $C_n^2 = 1 \times 10^{-14}\,\mathrm{m}^{-2/3}$, the DPS decreases to stability while the CPS is exactly the opposite to the DPS. All the channel capacity can reach the upper bound as long as the transmission power $P_{Tx}$ is large enough.

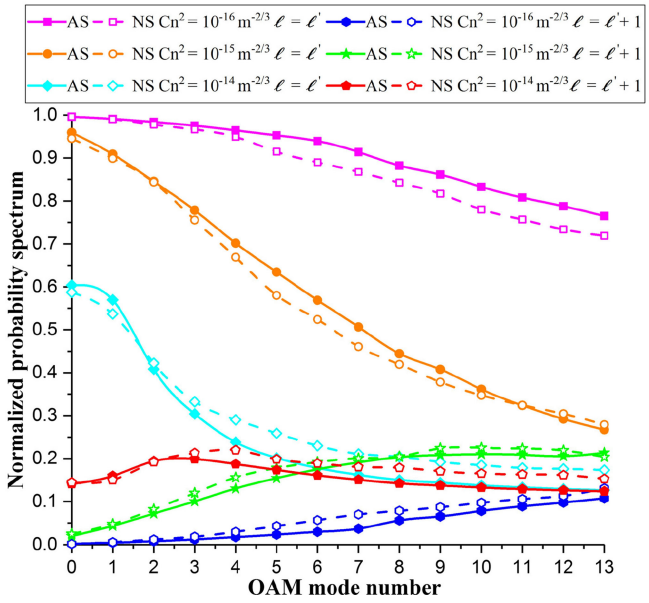


Fig. 8. The normalized DPS and CPS of the LOAMM system in atmospheric turbulence with the refractive-index structure constant $C_n^2 = 1 \times 10^{-16}$, $1 \times 10^{-15}$, $1 \times 10^{-14}$ m$^{-2/3}$ respectively, as a function of the OAM mode number. The propagation distance $L_d = 1000$ m and the parameter of aperture function $\alpha$ is chosen to contain the main lobe of FWs with different OAM modes.

Fig. 10 illustrates the comparisons between the aggregate capacity of the OAM-SDM system based on Bessel beams with the sets of $O_1$, $O_2$, $O_3$ and the LOAMM system with the sets of $U_1$, $U_2$. We first calculate the BER of each channel in the OAM-SDM system. It should be noted that the sizes of aperture function are analyzed in the condition of OP and SP, respectively. In the OP condition, the aperture sizes should be designed to contain the main lobe of the largest topological charge in the OAM-SDM system. In the SP condition, the main lobe of the waveforms with the largest OAM state should be contained. When the refractive-index constant $C_n^2 = 1 \times 10^{-16}$ m$^{-2/3}$, the crosstalk induced by turbulence from other transmitted OAM modes is low and the set $O_3$ with larger mode spacing suffers a higher power penalty. As the strength of turbulence increases, sets with lower mode spacing suffer a higher power penalty. Just as depicted in Fig. 10(b) and (c), in the condition of $C_n^2 = 1 \times 10^{-15}$ m$^{-2/3}$ and $C_n^2 = 1 \times 10^{-14}$ m$^{-2/3}$, sets $O_2$ and $O_3$ suffers the lowest power penalty, respectively. Based on the BER expressed in Fig. 10(a)–(c), the aggregate capacity of OAM-SDM system with three sets are calculated. It is shown that for small mode spacing, the performance of the OAM-SDM system is more perfect when the turbulence is weak. On the contrary, as the strength of turbulence becomes stronger, the set with larger mode spacing is more conspicuous. For the LOAMM system, the red curve denotes the OP condition and the yellow curve denotes the SP condition. It can be found from Fig. 10(d)–(f) that the LOAMM system has a better performance in the condition of OP.

In comparison with the LOAMM system, there is no obvious advantage between the two systems when the $C_n^2 \leq 1 \times 10^{-16}$ m$^{-2/3}$. However, as the strength of turbulence increases, the LOAMM system establishes significantly superiority over OAM-SDM system. Even in the case of $C_n^2 = 1 \times 10^{-14}$ m$^{-2/3}$, the aggregate capacity of OAM-SDM system with $O_1$ and $O_2$ cannot reach the saturation (4 bits/channels). It can be seen from Fig. 10(d)–(f) that the LOAMM system with smaller mode spacing suffers lower power penalty, which is consistent with the curves in Fig. 9(a)–(c). The results are primarily attributed to the fact that the LOAMM system is barely affected by the inter-model crosstalk. A reasonable explanation is that the LOAMM system has a greater advantage with smaller mode spacing sets. To a certain extent, the system can be designed even with the same OAM modes in different longitudinal intervals. Consequently, the spectral efficiency of the LOAMM system increases and the costs of receiver equipment for laser beams will reduce.

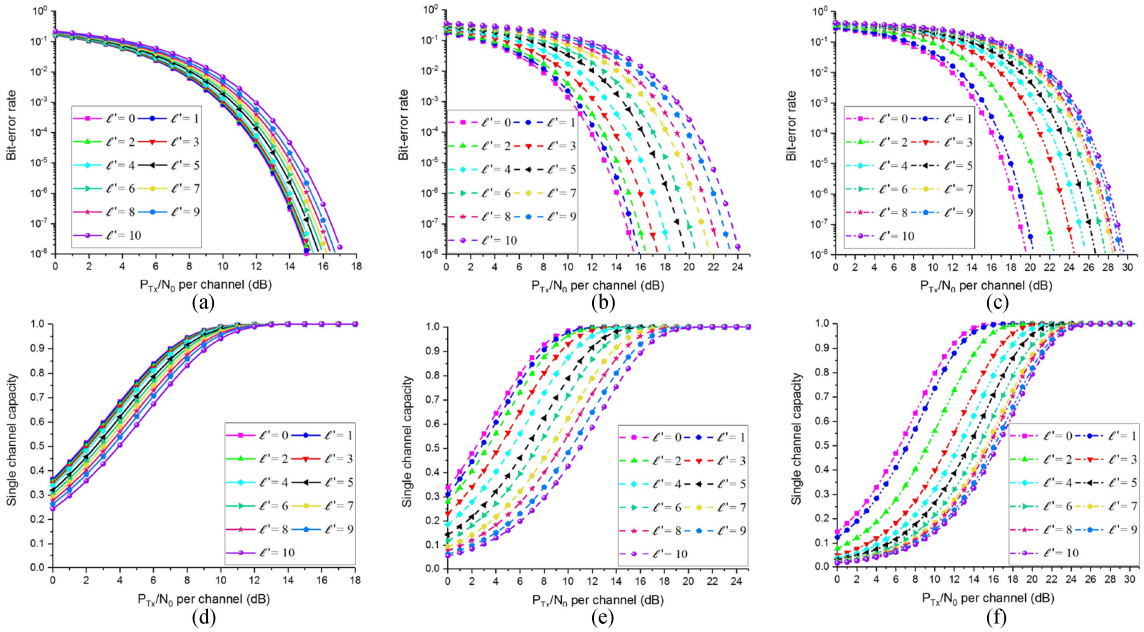


Fig. 9. The BER and channel capacity as a function of $P_{Tx}/N_0$ in single independent channel. The OAM mode ranges from 0 to +10, the refractive-index constant are $C_n^2 = 1 \times 10^{-16}$ for (a), (d), $C_n^2 = 1 \times 10^{-15}$ for (b), (e) and $C_n^2 = 1 \times 10^{-14}$ for (c), (f), other parameters are the same with Fig. 8.

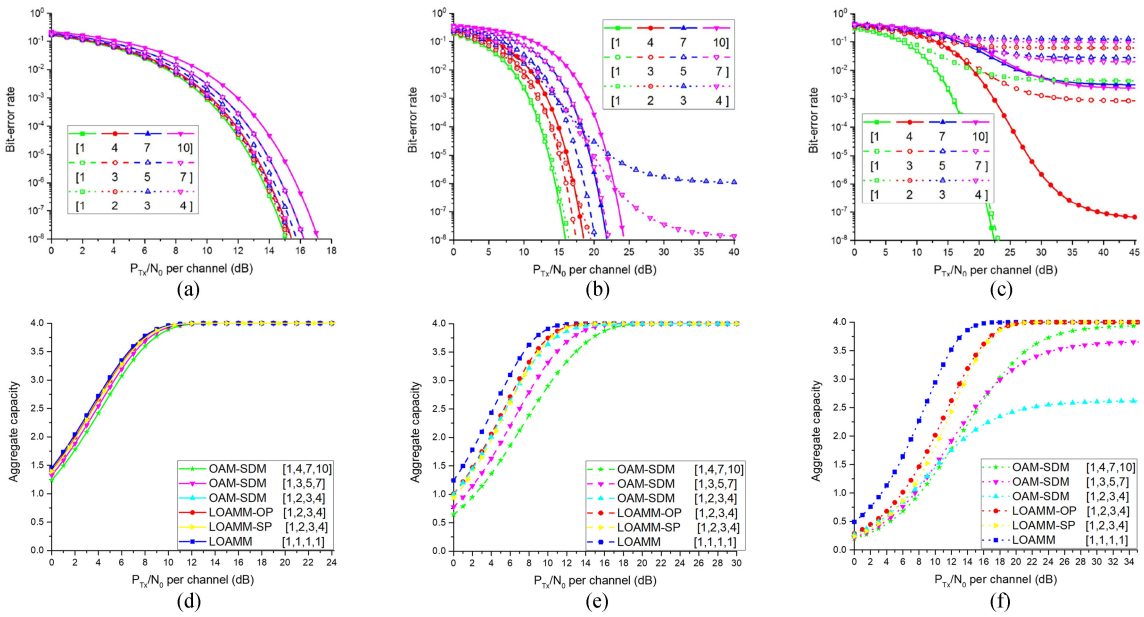


Fig. 10. The BER as a function of $P_{Tx}/N_0$ in traditional OAM-SDM system and the caparison of aggregate capacity between OAM-SDM systems with sets $O_1 = \{+1, +2, +3, +4\}$, $O_2 = \{+1, +3, +5, +7\}$, $O_3 = \{+1, +4, +7, +10\}$ and LOAMM systems with $U_1 = \{+1, +2, +3, +4\}$ for the condition of OP and SP and $U_2 = \{+1, +1, +1, +1\}$. The refractive-index constant is $C_n^2 = 1 \times 10^{-16}$ for (a), (d), $C_n^2 = 1 \times 10^{-15}$ for (b), (e) and $C_n^2 = 1 \times 10^{-14}$ for (c), (f), other parameters are the same with Fig. 8.

## 5. Conclusion

In conclusion, the model of average OAM mode density for the LOAMM system carried by FWs in isotropic atmospheric turbulence is developed by introducing split-step Fourier transform method based on multiple random phase screens. The influences of the propagation distance $L_d$, the refractive-index constant $C_n^2$, the parameter of aperture function $\alpha$, the number of Bessel beams $m$ and the OAM mode number on the normalized DPS and CPS are investigated. The results are reliable compared with the Rytov approximation. Obviously, the detection noise and crosstalk induced by turbulence remarkably affect the characteristics and channel capacity of OAM-based FSO communication systems. For the FWs, the increases of $L_d$, $C_n^2$ and OAM mode number indeed result in the degradation of DPS. In the condition of OP, the suitable size $\alpha$ can give rise to the increase of the DPS if the function contains the main lobe of FWs. The DPS can reach the maximum region when $m$ is close to its upper bound. Based on the BER of each channel, the aggregate capacity of OAM-SDM system and LOAMM system are calculated. The results indicate that in the circumstance that only the upper bound of capacity is considered, the LOAMM systems outperform the traditional OAM-SDM systems.

In the future, we will continue our work in expanding the LOAMM system for practical application in FSO communication systems through atmospheric turbulence.

## References


[1] M. I. Olmedo *et al.*, "Multiband carrierless amplitude phase modulation for high capacity optical data links," *J. Lightw. Technol.*, vol. 32, no. 4, pp. 798–804, Feb. 15, 2014.

[2] B. Liu, X. Xin, L. Zhang, and J. Yu, "109.92-Gb/s WDM-OFDMA UniPON with dynamic resource allocation and variable rate access," *Opt. Exp.*, vol. 20, no. 10, pp. 10552–10561, Apr. 2011.

[3] X. Xin, B. Liu, L. Zhang, and J. Yu, "40-Gb/s FSK modulated WDM-PON with variable-rate multicast overlay," *Opt. Exp.*, vol. 19, no. 13, pp. 12515–12523, Jun. 2011.

[4] G. Gibson *et al.*, "Free-space information transfer using light beams carrying orbital angular momentum," *Opt. Exp.*, vol. 12, pp. 5448–5456, Nov. 2004.

[5] J. Wang *et al.*, "Terabit free-space data transmission employing orbital angular momentum multiplexing," *Nature Photon.*, vol. 6, no. 7, pp. 488–496, Jul. 2012.

[6] S. Mi, T. Wang, G. Jin, and C. Wang, "High-capacity quantum secure direct communication with orbital angular momentum of photons," *IEEE Photon. J.*, vol. 7, no. 5, Oct. 2015, Art. no. 7600108.

[7] Y. Ren *et al.*, "Atmospheric turbulence effects on the performance of a free space optical link employing orbital angular momentum multiplexing," *Opt. Lett.*, vol. 38, no. 20, pp. 4062–4065, Oct. 2013.

[8] Y. Ren *et al.*, "Adaptive-optics-based simultaneous pre- and post-turbulence compensation of multiple orbital-angular-momentum beams in a bidirectional free-space optical link," *Optica*, vol. 1, no. 6, pp. 376–382, Dec. 2014.

[9] H. Chang *et al.*, "Adaptive optics compensation of orbital angular momentum beams with a modified Gerchberg–Saxton-based phase retrieval algorithm," *Opt. Commun.*, vol. 405, pp. 271–275, Dec. 2017.

[10] H. Huang *et al.*, "Crosstalk mitigation in a free-space orbital angular momentum multiplexed communication link using 4x4 MIMO equalization," *Opt. Lett.*, vol. 39, no. 15, pp. 4360–4363, Aug. 2014.

[11] M. Cheng, L. Guo, J. Li, and Y. Zhang, "Channel capacity of the OAM-based free-space optical communication links with Bessel–Gauss beams in turbulent ocean," *IEEE Photon. J.*, vol. 8, no. 1, Feb. 2016, Art. no. 7901411.

[12] X. Sun and I. B. Djordjevic, "Physical-layer security in orbital angular momentum multiplexing free-space optical communications," *IEEE Photon. J.*, vol. 8, no. 1, pp. 1–10, Feb. 2016.

[13] J. A. Anguita, M. A. Neifeld, and B. Vasic, "Turbulence-induced channel crosstalk in an orbital angular momentum-multiplexed free-space optical link," *Appl. Opt.*, vol. 47, no. 13, pp. 2414–2429, May 2008.

[14] G. Xie *et al.*, "Performance metrics and design considerations for a free-space optical orbital-angular-momentum–multiplexed communication link," *Optica*, vol. 2, no. 4, pp. 357–365, Apr. 2015.

[15] A. E. Willner *et al.*, "Design challenges and guidelines for free-space optical communication links using orbital-angular-momentum multiplexing of multiple beams," *J. Opt.*, vol. 18, no. 7, Jun. 2016, Art. no. 074014.

[16] M. Zamboni-Rached, "Stationary optical wave fields with arbitrary longitudinal shape by superposing equal frequency Bessel beams: Frozen waves," *Opt. Exp.*, vol. 12, no. 17, pp. 4001–4006, Aug. 2004.

[17] E. G. P. Pachon, M. Zamboni-Rached, A. H. Dorrah, M. Mojahedi, M. R. R. Gesualdi, and G. G. Cabrera, "Architecting new diffraction-resistant light structures and their possible applications in atom guidance," *Opt. Exp.*, vol. 24, no. 22, pp. 25403–25408, Oct. 2016.

[18] L. A. Ambrosio and M. Zamboni-Rached, "Analytical approach of ordinary frozen waves for optical trapping and micromanipulation," *Appl. Opt.*, vol. 54, no. 10, pp. 2584–2593, Apr. 2015.

[19] L. A. Ambrosio and M. Zamboni-Rached, "Optical forces experienced by arbitrary-sized spherical scatterers from superpositions of equal-frequency Bessel beams," *J. Opt. Soc. Amer. B*, vol. 32, no. 5, pp. 37–46, May 2015.

[20] A. H. Dorrah, M. Zamboni-Rached, and M. Mojahedi, "Controlling the topological charge of twisted light beams with propagation," *Phys. Rev. A*, vol. 93, no. 6, pp. 063864(1)–063864(6), Jun. 2016.

[21] T. Doster and A. T. Watnik, "Laguerre–Gauss and Bessel–Gauss beams propagation through turbulence: Analysis of channel efficiency," *Appl. Opt.*, vol. 55, no. 36, pp. 10239–10246, Aug. 2016.
[22] M. Charnotskii, "Extended Huygens-Fresnel principle and optical waves propagation in turbulence: Discussion," *J. Opt. Soc. Amer. A*, vol. 24, no. 17, pp. 19713–19727, Jul. 2015.
[23] C. Chen and H. Yang, "Characterizing the radial content of orbital-angular-momentum photonic states impaired by weak-to-strong atmospheric turbulence," *Opt. Exp.*, vol. 32, no. 7, pp. 1357–1365, Jul. 2015.
[24] J. D. Schmidt *Numerical Simulation of Optical Wave Propagation With Examples in MATLAB*. Bellingham, WA, USA: SPIE, 2010.
[25] J. Durnin, J. J. Miceli Jr., and J. H. Eberly, "Diffraction-free beams," *Phys. Rev. Lett.*, vol. 58, no. 15, pp. 1499–1501, Apr. 1987.
[26] D. McGloin and K. Dholakia, "Bessel beams: Diffraction in a new light," *Contemp. Phys.*, vol. 46, no. 1, pp. 15–28, Jan. 2005.
[27] S. M. Flatt´e, G. Y. Wang, and J. Martin, "Irradiance variance of optical waves through atmospheric turbulence by numerical simulation and comparison with experiment," *J. Opt. Soc. Amer.*, vol. 10, no. 11, pp. 2363–2370, Nov. 1993.
[28] M. I. Charnotskii, "Common omissions and misconceptions of wave propagation in turbulence: Discussion," *J. Opt. Soc. Amer. A*, vol. 29, no. 5, pp. 711–721, May 2012.
[29] L. C. Andrews, S. Vester, and C. E. Richardson, "Analytic expressions for the wave structure function based on a bump spectral model for refractive index fluctuations," *J. Mod. Opt.*, vol. 40, no. 5, pp. 931–938, May 1993.
[30] L. C. Andrews and R. L. Phillips, *Laser Beam Propagation Through Random Media*. Bellingham, WA, USA: SPIE, 2005.
[31] Y. Yuan, T. Lei, S. Gao, X. Weng, L. Du, and X. Yuan, "The orbital angular momentum spreading for cylindrical vector beams in turbulent atmosphere," *IEEE Photon. J.*, vol. 9, no. 2, pp. 1–10, Apr. 2017.
[32] M. Cheng, L. Guo, J. Li, Q. Huang, Q. Cheng, and D. Zhang, "Propagation of an optical vortex carried by a partially coherent Laguerre-Gaussian beam in turbulent ocean," *Appl. Opt.*, vol. 55, no. 17, pp. 4642–4648, Jun. 2016.
[33] X. Yin, H. Sang, X. Cui, H. Chang, L. Li, and G. Wu, "Offset tolerance of an orbital angular momentum optical communication system with angular deflection," *Opt. Commun.*, vol. 393, pp. 34–39, Jun. 2017.
[34] N. Zhao, X. Li, G. Li, and J. M. Kahn, "Capacity limits of spatially multiplexed free-space communication," *Nature Photon.*, vol. 9, no. 12, pp. 822–826, Dec. 2015.
[35] Y. Zhao, X. Zhong, G. Ren, S. He, and Z. Wu, "Capacity of arbitrary-order orbital angular momentum multiplexing system," *Opt. Commun.*, vol. 387, pp. 432–439, Mar. 2017.
[36] X.-z. Cui, X.-l. Yin, H. Chang, Z.-C. Zhang, Y.-J. Wang, and G.-H. Wu, "A new method of calculating the orbital angular momentum spectra of Laguerre–Gaussian beams in channels with atmospheric turbulence," *Chin. Phys. B*, vol. 26, no. 11, May 2017, Art. no. 114207.
[37] P. Birch, I. Ituen, R. Young, and C. Chatwin, "Long-distance Bessel beam propagation through Kolmogorov turbulence," *J. Opt. Soc. Amer. A*, vol. 32, no. 21, pp. 2066–2073, Nov. 2015.